Quantifying desorption and rearrangement rates of carbon monoxide on a PEM fuel cell electrode

Vijay A. Sethuraman [1,2], Balasubramanian Lakshmanan [3], John W. Weidner [*]

Center for Electrochemical Engineering, Department of Chemical Engineering, University of South Carolina, Columbia, SC 29208, USA

ARTICLE INFO

ABSTRACT

A simple procedure to quantify the rates of carbon monoxide (CO) desorption from, and simultaneous rearrangement on, supported platinum fuel cell electrode (Pt on Vulcan XC-72R) is reported. The surface coverage of CO on Pt electrode in equilibrium with bulk CO was measured from the anodic peaks in the CO stripping voltammogram. The decline in these surface coverages due to desorption and rearrangement, once CO was replaced by N_2 in the gas phase was recorded and used in conjunction with a kinetic model to quantify the respective rates. Two distinct CO oxidation peaks observed in the voltammogram due to the oxidation of two distinct ad-species, namely weakly and strongly adsorbed CO (CO_{ad}^I and CO_{ad}^{II}), were baseline corrected and deconvoluted using a bimodal Gaussian distribution. Saturation surface coverage of CO_{ad}^I decreased with increasing temperature, while the opposite was true for CO_{ad}^{II}. Rearrangement from CO_{ad}^{II} to CO_{ad}^I was faster than the desorption rate of either CO species. The desorption rate of CO_{ad}^{II} was at least an order of magnitude lower than that of CO_{ad}^I molecules at all temperatures studied. The activation energies for desorption of CO_{ad}^I and CO_{ad}^{II} were estimated to be 24.08 and 27.99 kJ/mol, respectively. The activation energy for rearrangement from CO_{ad}^I to CO_{ad}^{II} was 35.23 kJ/mol and that from CO_{ad}^{II} to CO_{ad}^I was 27.55 kJ/mol.

© 2009 Elsevier Ltd. All rights reserved.

1. Introduction

Carbon monoxide (CO) kinetics on polycrystalline Pt electrodes is of considerable interest because of CO poisoning in PEM fuel cells operating on hydrogen derived from hydrocarbons (reformate feed) [1,2]. Though there are myriad published studies on CO kinetics on fuel cell catalysts (Pt, PtRu, etc.) such as poisoning mechanisms [3], performance losses and ways to mitigate such losses [4,5], studies on *in situ* estimation of CO kinetics (such as rates of adsorption, desorption and electro-oxidation) on PEM fuel cell electrodes is scarce and have received very minimal attention. There are few spectroscopic studies [6,7] by Korzeniewski et al. that attempt to estimate desorption rates of CO from Pt electrodes but accurate kinetic analysis using spectroscopic methods is generally not possi-

ble due to optical interferences. Motivation to estimate a consistent set of parameters describing CO kinetics on a PEM fuel cell electrode is two-fold: for modeling CO tolerance in reformate-fed PEM fuel cells and for the design and optimization of an electrochemical CO filter [8,9] developed in our laboratory. McEwen et al. developed a comprehensive theory of adsorption, desorption and rearrangement kinetics of CO on Pt(1 1 1) using Monte Carlo methods and report relevant kinetic parameters [10]. However, they cannot be directly used in the context of CO kinetics on PEM fuel cell electrodes because the fuel cell electrodes are made with supported Pt nanoparticles. Current models [11–13] for PEM fuel cells operating on reformate feed assume either Langmuir–Hinshelwood or Temkin isotherms for describing adsorption and desorption kinetics of CO on Pt. The reaction rate constants in these Springer type [12] models are estimated by fitting the model to overall performance data and vary widely. In this work, we report a simple *in situ* procedure using cyclic voltammetry (CV) on a functional PEM fuel cell electrode to measure CO desorption and rearrangement rates from a PEM fuel cell electrode (Pt supported on carbon). The amount of CO adsorbed on a PEM fuel cell electrode was measured from the charge corresponding to the oxidation of the adsorbed CO during CV, i.e., by integrating the dual anodic peaks observed in the CV.

Gilman [14,15] first showed the existence of two anodic peaks in CO CVs and it is generally agreed that when CO is adsorbed on

* Corresponding author at: Department of Chemical Engineering, Swearingen Engineering Center, University of South Carolina, 301 Main Street, Columbia, SC 29208, USA. Tel.: +1 803 777 3207; fax: +1 803 777 8265.

E-mail address: weidner@cec.sc.edu (J.W. Weidner).

[1] International Society of Electrochemistry Active Member.

[2] Present address: Environmental Energy Technology Division, MS 70-R0108B, Lawrence Berkeley National Laboratory, Berkeley, CA 94720, USA.

[3] Present address: General Motors Fuel Cell Activities, 10 Carriage Street, Honeoye Falls, NY 14472, USA.

Pt under steady-state conditions and at potentials in the neighborhood of hydrogen reversible potential, two anodic peaks appear in the stripping voltammogram [16–21]. The spectroscopic nature of CO adsorption on Pt was studied in the early 1950s by Eischens and Pliskin [22] using infrared techniques, where they showed evidence for two types of CO structures adsorbed on Pt supported on cabosil and alumina. The spectroscopic nature of the adsorbed CO has been well studied since then using a variety of techniques and was shown to be dependent on the surface coverage, the potential of the electrode at which CO was adsorbed [23–25] and temperature [26,27]. Surface coverage of one of the CO species was shown to be higher than the other in surfaces adsorbed at higher potentials (>0.5 V vs. SHE) [23]. In addition, the kinetics of CO electro-oxidation on Pt nanoparticles was also shown to depend on the particle size [28–32], catalyst loading on the support [33], crystalline defects [34] and structure [35,36]. Though no clear correlation exists in the literature between nature of CO adsorption onto Pt nanoparticles and their oxidation potentials [37], majority of the studies attribute the peak-splitting observed in the CO stripping voltammetry for carbon supported Pt nanoparticles to particle size [29,35,38]. If the shape of the Pt nanoparticle is assumed to be a cubo-octahedral structure consisting of (1 1 1) and (1 0 0) facets bound by edge atom rows similar to the topmost rows of (1 1 0) surface, then benchmark studies on single-crystal surfaces may be used to understand the nature of CO adsorption on these nanoparticles [39,40].

The first step towards using results from single-crystal studies on Pt nanoparticles would be to arrive at a surface distribution of crystallographic faces on an averaged particle size. This was accomplished by using Van Hardeveld's classical work on the statistics of surface atoms and surface sites on metallic particles [41,42]. For the average Pt particle size of 5 nm (for the batch of 40 wt% Pt/C ETEK catalyst we used in this study, see Fig. 1 and assuming the shape of the Pt particle to be cubo-octahedral) [29], we estimate that ∼70% of the surface is Pt(1 1 1) with the rest Pt(1 0 0) and edge and corner sites [43]. Markovic et al. studied CO oxidation on Pt(1 1 1) in acid solutions at room temperature using voltammetry on a rotating disc electrode (RDE) in conjunction with *in situ* surface X-ray diffraction (XRD) measurements. They reported the presence of weakly (CO_{ad}^{I}) and strongly (CO_{ad}^{II}) bound CO species and that the former forms at saturation coverage and assumes a p(2 × 2) structure containing three CO molecules per unit cell (0.75 CO/Pt) and its oxidative removal was accompanied by simultaneous relaxation of CO adlayer with the remaining CO_{ad}^{II} (0.6 CO/Pt) assuming a new bonding state [44]. The electro-oxidation of CO_{ad}^{I} and CO_{ad}^{II} were respectively attributed to the first and second peaks observed in the CO stripping voltammograms. We therefore use these CO/Pt values to calculate the number of Pt sites with weakly and strongly adsorbed CO molecules based on the respective coulombic charges obtained from the CO stripping voltammograms. Though these conclusions are valid only for Pt(1 1 1) surfaces, we use these results in analyzing CO desorption and rearrangement kinetics in this study because the majority of the surface is Pt(1 1 1).

The objective of this work is not to theorize CO adsorption and desorption mechanisms on Pt nanoparticles but to develop a procedure to quantify desorption and rearrangement rates of CO_{ad}^{I} and CO_{ad}^{II} species, as indicated by voltammetry data. This is accomplished by first measuring the surface coverages of CO_{ad}^{I} and CO_{ad}^{II} after saturation with CO in the gas phase. The observed decline in these surface coverages due to desorption and rearrangement, once CO was replaced by N_2 in the gas phase, were then measured as a function of desorption time. The relevant rate constants were then estimated by fitting this data to a kinetic model. The respective activation energies were estimated by repeating these procedures at different temperatures.
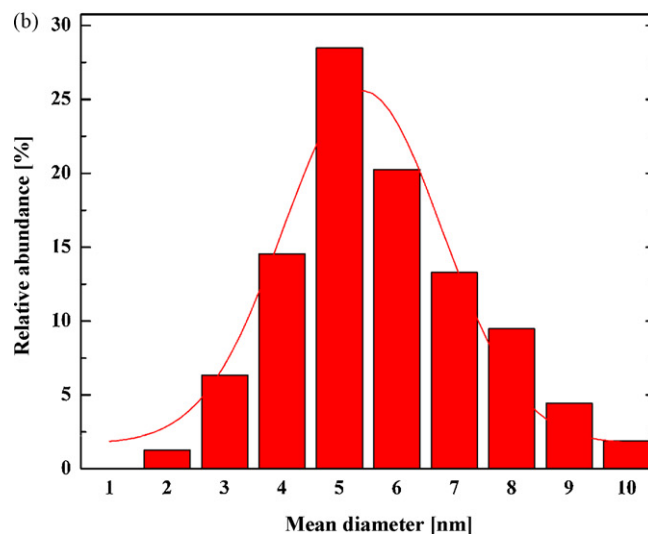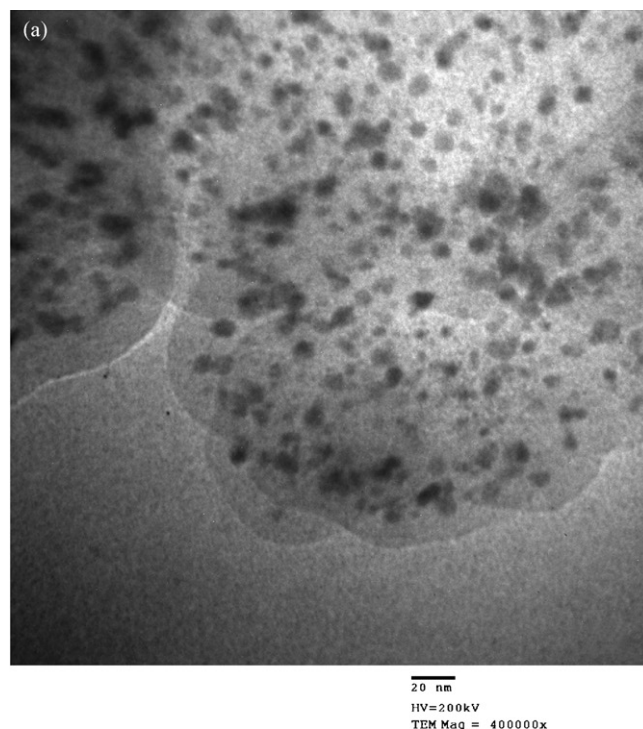

Fig. 1. (a) Bright-field high-resolution transmission electron micrograph of 40% Pt on carbon (Vulcan XC-72R) catalyst used in this study. The Pt particles appear darker relative to the carbon support. The particle size distribution of the catalyst was determined using transmission electron microscopy (TEM, Hitachi H-8000, Japan). (b) Histogram of mean particle diameter, in the size range of 0–10 nm shown along with a Gaussian distribution fit. The mean diameter was 5.4 ± 0.15 nm and the standard deviation was 1.667 nm.

2. Experimental

2.1. Fuel cell electrode fabrication

Pt catalyst ink with 75% catalyst and 25% Nafion® (dry solids content) was prepared with commercially available 40 wt% Pt on Vulcan XC-72R E-TEK® catalyst (PEMEAS Fuel Cell Technologies, Somerset, NJ). Nafion® in the form of perfluorosulfonic acid–PTFE copolymer (5% w/w solution, Alfa Aesar, Ward Hill, MA) was used. The catalyst ink was sprayed onto gas diffusion layers (ELAT® GDL, 10 cm² active area, PEMEAS Fuel Cell Technologies, Somerset, NJ) with N_2 brush (Paasche Airbrush Company, Chicago, IL), air dried

for 30 min and then dried under vacuum (381 mmHg) at 110 °C for 10 min to evaporate any remaining solvent. This process was repeated until a catalyst loading of 0.5 mg Pt/cm^2 was achieved. Two such catalyst coated GDLs were then bonded to either side of a pretreated Nafion® 112 membrane (Alfa Aesar, Ward Hill, MA) by hot pressing (140 °C), for 2 min at 3450 kPa to make a membrane electrode assembly (MEA). The MEA was then assembled into a fuel cell with single channel serpentine flow field plates (Fuel Cell Technologies Inc., Albuquerque, NM). The cell was operated at 0.4 A/cm^2 for 8 h at 70 °C and 101.325 kPa with a flow of 0.12 standard liters per minute (SLM) H$_2$ and 0.36 SLM air on the anode and cathode sides, respectively. Polarization (*V–I*) curves were recorded and compared to a baseline *V–I* curve to confirm that the fuel cell was working properly. All pure gases (except for industrial grade air) used in the experiments were obtained from Air Products and were certified ultra high purity (UHP).

2.2. CO coverage

After the fuel cell conditioning process, the cathode gas was switched to H$_2$ at 0.05 SLM, which acted as counter and reference electrode (i.e., dynamic hydrogen electrode, DHE). All potentials reported here refer to this electrode. The anode gas was switched to N$_2$ at 0.1 SLM. After allowing the N$_2$ to purge through the fuel cell channels, flow was switched to 476 ppm CO in N$_2$ (hereafter referred to as CO/N$_2$) at 0.10 SLM for 300 s. This exposure time was approximately twice the residence time of the gas channels and ensured complete exposure of the Pt to CO. Nitrogen flow was restored after this exposure. An exposure time of 300 ± 100 s did not affect the results shown here and that electrode reaches a steady-state condition (i.e., the surface coverage did not change with time; see Section 3 for Fig. 4). After a wait period of 30 s, the cell was held at a constant potential of 50 mV for 25 s followed by a CV at the rate of 20 mV s^{-1} from 50 to 1150 mV and back to 50 mV. This scan rate was chosen because higher scan rates (i.e., >50 mV s^{-1}) caused the two distinct peaks to collapse onto each other and lower scan rates (i.e., <1 mV s^{-1}) took too long and the timescales were such that CO desorption interfered with the measurement of CO surface coverage. Experiments were conducted using a M263A potentiostat/galvanostat (Princeton Applied Research Inc., Oak Ridge, TN) and ECHEM® software made by EG&G. The area under the CO oxidation peak, Q_{CO}, in the potential window 600–850 mV relative to the background current was used to calculate the amount of CO oxidized, which was taken to be the amount of CO adsorbed. The area under H$_2$ desorption peak, Q_H, in the potential window 50–350 mV corrected for the background was also measured. The experiment was repeated for various durations of CO/N$_2$ exposure. Between each experiment, another CV was performed on the electrode and the resulting CV overlapped with the background, confirming that all adsorbed CO was oxidized in the first cycle.

Fig. 2 shows a representative CV before and after CO adsorption. The dotted and the solid lines correspond to a clean and a CO adsorbed electrode, respectively. The broad peak between 50 and 400 mV and the two distinct peaks between 600 and 1000 mV correspond to hydrogen (Pt–H → Pt + H$^+$ + e$^-$) and CO oxidation (Pt$_x$–CO + Pt$_x$–H$_2$O → 2xPt + CO$_2$ + 2H$^+$ + 2e$^-$; *x* = *h*, *k*) with their electrochemical areas represented by Q_H and Q_{CO}, respectively. The areas under hydrogen and CO peaks were 598 mC and 880 mC, respectively. The charge under the voltammetric peaks for hydrogen desorption, corrected for double layer charging was assumed to correspond to one hydrogen atom on each Pt atom on the surface. Oxidation current from CO covered electrode in the 50–400 mV potential window was used as the baseline for estimating the coulombic area of hydrogen desorption. Current from a clean electrode in the 500–800 mV potential window was used as the baseline for estimating the coulombic area corresponding to CO oxi-
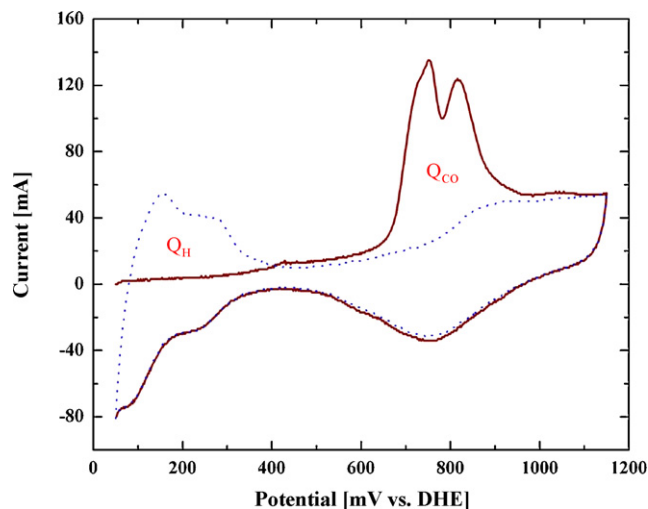

Fig. 2. CV obtained on a 40% Pt supported on XC-72R Nafion® composite electrode after exposure to 476 ppm CO in N$_2$ for 300 s at 25 °C and 101.325 kPa. Q_H and Q_{CO} correspond to the amount of H$_2$ and CO oxidized, respectively. The dotted and the solid lines correspond to CVs from a clean and a CO covered (steady-state coverage) electrode, respectively.

dation. This procedure is similar to that of Arenz et al. [28]. It should be noted that the coulometric procedure described by Gómez et al. [45] to evaluate charge due to CO oxidation from voltammograms is applicable only where there is pseudo-capacitance through adsorption of anions present in the electrolyte.

2.3. CO desorption

To extract the rate of CO desorption from the Pt/C electrodes the amount of CO remaining on the electrode was determined as a function of desorption time. The electrode was exposed to CO/N$_2$ for 300 s after which the flow on the anode side was switched to N$_2$. A CV was conducted after waiting for a specific duration called as desorption time. The cell was at open circuit (*ca.* 80 mV vs. DHE) during CO exposure and desorption steps. The area under the CO oxidation peaks in the resulting CVs was estimated as outlined below. The adsorption, desorption and voltammetry steps were repeated for various desorption times and temperatures.

The CVs obtained on a CO covered electrode were baseline corrected and the peaks were deconvoluted with a bimodal Gaussian distribution using commercially available software (Tablecurve2D®, Systat® Software Inc., San Jose, CA). The general form of bimodal Gaussian distribution used for this case is given as:

$$I = ae^{-((V-b)/c)^2} + de^{-((V-e)/f)^2} \qquad (1)$$

The process for deconvoluting the two peaks involved the following steps: baseline corrected data was imported into the Tablecurve2D®, data was filtered to represent the voltage window of interest, the filtered data was fit to a general form of a bimodal Gaussian distribution and the fitting parameters (*a*, *b*, . . ., *f*) were iterated to maximize the R^2 and *F*-value. The result of this process for the CV shown in Fig. 2 is given in Fig. 3. The resulting fit for all deconvolutions had an R^2 greater than 0.98 and the deconvolution parameters were estimated with a 95% or higher confidence interval. The deconvolution in Fig. 3 shows two overlapping peaks with a peak height of about 100 mA and 75 mA for the first and second peaks, respectively. The miniscule shoulder observed on the left side of the first peak was routinely observed on most of the CVs conducted at lower temperatures (<40 °C). This could be due to a third kind of adsorption, i.e., CO on a hollow site. This shoul-
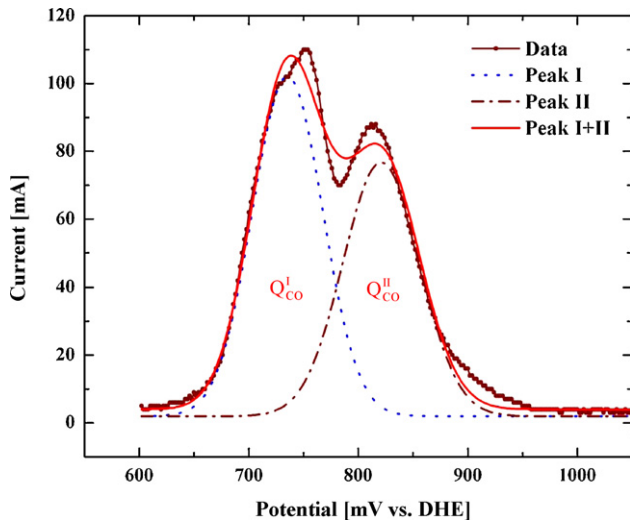
Fig. 3. Baseline corrected CO oxidation peaks (from Fig. 2) deconvoluted using bimodal Gaussian distribution (Eq. (1)) shown along with the sum of two peaks. The lines (dot, dot-dash, and solid line) correspond to peaks I, II and I+II, respectively. The following parameters (Eq. (1)) were used for this fit: $a = 100.13$, $b = 735.42$, $c = 45.28$, $d = 74.75$, $e = 820.86$ and $f = 49.4$.

der or the 'third peak' was treated as oxidation of a weakly bound CO molecule in this work. The sum of these two peaks was fit to the experimental data with an R^2 greater than 0.99. The only purpose for describing the CO coverage through a bimodal Gaussian distribution was to estimate the charge under the peaks. It was not to establish this distribution as the true representation of what is happening at the surface. Statistically we achieved an excellent fit and therefore any other assumed distributions would not have been any more accurate.

2.4. Model development

The first peak occurring at a lower potential was assigned to the oxidation of weakly adsorbed CO molecules (CO_{ad}^{I}) and the area under this peak was designated as Q_{CO}^{I}. Similarly, the second peak occurring at a higher potential was assigned to the oxidation of strongly adsorbed CO molecules (CO_{ad}^{II}) and the area under this peak was designated as Q_{CO}^{II}. It must be noted here that the hydroxyl species (OH_{ads}) play an important role in the electro-oxidation of CO_{ads} and thus in principle could influence the shape of the two CO oxidation peaks. This is because OH_{ads} is an intermediate in the rate-determining step for CO oxidation ($CO_{ad} + OH_{ad} \rightarrow CO_2 + H^+ + e^-$) [46]. However, the formation of OH_{ads} on Pt occurs at a much faster rate compared to the electro-oxidation of either of the CO species and therefore not kinetically limiting [47,48]. The fraction of Pt sites covered by CO_{ad}^{I} and CO_{ad}^{II} were expressed respectively as:

$$\theta_{CO}^{I} = \frac{h_I Q_{CO}^{I}}{\left[h_I Q_{CO}^{I} + h_{II} Q_{CO}^{II}\right]_{max}} \tag{2}$$

$$\theta_{CO}^{II} = \frac{h_{II} Q_{CO}^{II}}{\left[h_I Q_{CO}^{I} + h_{II} Q_{CO}^{II}\right]_{max}} \tag{3}$$

where $\left[h_I Q_{CO}^{I} + h_{II} Q_{CO}^{II}\right]_{max}$ was the maximum area under the CO peaks. The parameters h_I and h_{II} correspond to the reciprocal of number of CO molecules adsorbed per Pt site (CO/Pt) for CO_{ad}^{I} and CO_{ad}^{II}, respectively. Values of $1/h_I = 0.75$ and $1/h_{II} = 0.6$ based on data from Markovic et al. [44] were used. The fraction of Pt sites covered by CO molecules was the sum of fractional coverage of CO_{ad}^{I} and

CO_{ad}^{II} given by equation (4):

$$\theta_{CO} = \theta_{CO}^{I} + \theta_{CO}^{II} \tag{4}$$

The fraction of the vacant sites, θ_v was obtained from the site balance:

$$\theta_v = 1 - \theta_{CO} = 1 - \theta_{CO}^{I} - \theta_{CO}^{II} \tag{5}$$

Good agreement on site balance based on Q_H and Q_{CO} was reached by using CO/Pt values reported by Markovic et al. (i.e., 0.75 CO/Pt for Q_{CO}^{I} and 0.6 CO/Pt for Q_{CO}^{II}) along with the fractional coverage obtained from the deconvolution results. The value of $\left[h_I Q_{CO}^{I} + h_{II} Q_{CO}^{II}\right]_{max}$ was within 5% of $2 Q_H^0 \big|_{max}$ indicating slightly less than a monolayer coverage of CO on the Pt/C electrodes at maximum coverage (see Fig. 2).

CO adsorption, desorption and rearrangement proceed through the following reaction scheme, consistent with previous observation of dual modes of adsorption.

$$CO + Pt \underset{k_{-1}}{\overset{k_1}{\rightleftharpoons}} CO_{ad}^{I} \tag{6}$$

$$k_{-3} \uparrow\downarrow k_3 \tag{7}$$

$$CO + Pt \underset{k_{-2}}{\overset{k_2}{\rightleftharpoons}} CO_{ad}^{II} \tag{8}$$

Reactions (6) and (8) correspond to the adsorption and desorption of CO_{ad}^{I} and CO_{ad}^{II}, respectively. Note that the Pt sites in these reactions are not meant to be stoichiometrically balanced. Reaction (7) corresponds to the rearrangement between the weakly and strongly bound CO molecules. Spectroscopic proof of surface equilibrium between CO_{ad}^{II} and CO_{ad}^{I} has been reported before [49]. The following general assumptions were made for developing the kinetic model:

(1) All Pt sites were assumed equivalent.
(2) Pt sites did not change during the experiments. Though the applied potential during CV sweeps routinely exceeded the equilibrium potential for Pt dissolution ($\sim$1.0 V vs. DHE), Pt sites were assumed not to dissolve, migrate or ripen for the duration of the experiment. This is a valid assumption because of the duration of the applied potential, which was of the order of few minutes as opposed to the time constant for Pt dissolution and migration, which was shown to be at least two orders of magnitude higher [50].
(3) Isothermal conditions exist; and
(4) The reactions were assumed first order with respect to reactants (i.e., CO and Pt sites), consistent with literature [51–53].

The material balance for the surface coverage of Pt sites during desorption and rearrangement of CO_{ad}^{I} and CO_{ad}^{II} are given by Eqs. (9) and (10), respectively,

$$\frac{d\theta_{CO}^{I}}{dt} = -k_{-1}\theta_{CO}^{I} - \left(\frac{1}{h_{II}} - \frac{1}{h_I}\right) k_3 \theta_{CO}^{I}\theta_v + k_{-3}\theta_{CO}^{II} \tag{9}$$

$$\frac{d\theta_{CO}^{II}}{dt} = -k_{-2}\theta_{CO}^{II} + \left(\frac{1}{h_{II}} - \frac{1}{h_I}\right) k_3 \theta_{CO}^{I}\theta_v - k_3 \theta_{CO}^{II} \tag{10}$$

For $h_I < h_{II}$. Desorption and the rearrangement rate constants were estimated using data obtained from the desorption experiments.

2.5. Parameter estimation

Eqs. (5), (9) and (10) were solved with k_{-1}, k_{-2}, k_3, and k_{-3} as parameters using the known initial surface coverages of the two CO species and the total CO surface coverage versus time

Table 1
Estimated values of the parameters and the corresponding confidence intervals obtained at 50 °C.

Parameter	Value	Confidence
k_{-1}	4.475×10^{-5} s^{-1}	$\pm 5.024 \times 10^{-4}$
k_{-2}	1.029×10^{-5} s^{-1}	$\pm 5.024 \times 10^{-4}$
k_3	2.063×10^{-5} s^{-1}	$\pm 2.285 \times 10^{-4}$
k_{-3}	7.809×10^{-5} s^{-1}	$\pm 5.024 \times 10^{-4}$

data. The Levenberg–Marquardt method [54], a non-linear parameter estimation procedure, was used to estimate these parameters. Numeric Dsolve® subroutines in Maple® (Maplesoft®, Waterloo, ON, Canada) were used to solve the differential equations. Estimated values of the parameters and the corresponding confidence intervals obtained at 50 °C are given in Table 1. The activation energies were estimated from data obtained by repeating the experiments at different temperatures and by fitting the estimated rate constants to the form:

$$k_n = k_n^0 \exp\left(\frac{-E_a}{RT}\right) \qquad (11)$$

where E_a was the corresponding activation energy.

3. Results and discussion

Fig. 4 shows CVs obtained on a Pt electrode with N$_2$ in the gas phase after exposure to 476 ppm CO in N$_2$ for different exposure times and for a clean Pt electrode. The amount of CO adsorbed was equal to the amount fed for all exposure times below 300 s. The CO adsorption on Pt in this system was transport limited (i.e., limited by the amount fed) and an implication of this was that the adsorption rate constants (k_1 and k_2) could not be reliably measured. The amount of CO adsorbed and the nature of oxidation peaks did not change for exposure times greater than 300 s. For example, the CVs corresponding to exposure times of 300 and 450 s shown in Fig. 4 overlap.

Fig. 5 shows some of the CVs from a set of CVs obtained on Pt electrode after exposure to 476 ppm CO in N$_2$ at 0.10 SLM for 300 s as a function of temperature. With the increase in temperature, the CO peak shifts towards lower potential. For example, the potential corresponding to the peak current decreased from 609 to 559 mV when the temperature increased from 70 to 90 °C. Conversely, the peak current increased from 770 to 970 mA for the same increase in tem-
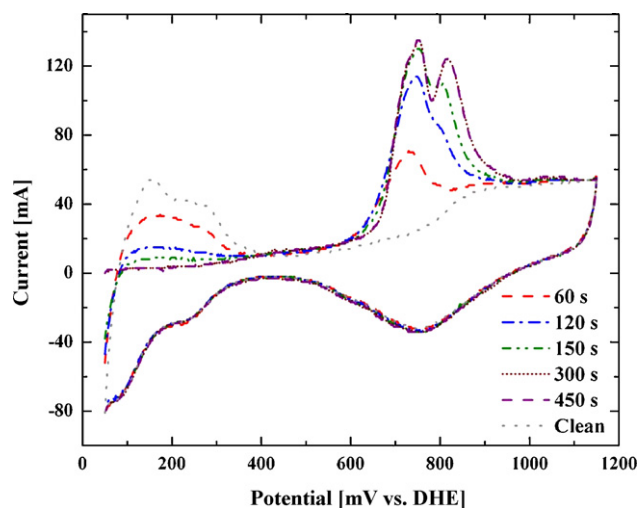

Fig. 5. CVs obtained on a Pt composite electrode after exposure to 476 ppm CO in N$_2$ for 300 s. The experiments were conducted at 101.325 kPa and different temperatures as indicated in the legend.

perature mentioned above. Both phenomena are well documented in the literature [55]. However, the change in the peak structure with increase in temperature, as seen in Fig. 5, had never been discussed before in the literature. It is possible that the temperature dependent electro-oxidation kinetics could be different for CO$_{ad}^I$ and CO$_{ad}^{II}$ but a detailed analysis along these lines is beyond the scope of this article. These voltammograms are reflective of the initial surface coverages and not due to the rearrangement between the two CO species. This is because, the rearrangement rates are slower and, as will be showed later, are typically of the order of desorption rates. Fig. 6 shows the surface coverages of CO$_{ad}^I$ and CO$_{ad}^{II}$ obtained from the set of CVs shown in Fig. 5. These represent the initial CO coverage for the fit to the rate expressions given by (9) and (10). The sum of these coverages (Eq. (4)) was 1 ± 0.05, which is expected because the anodic reaction in a functional PEM fuel cell with Pt anode completely shuts off at these temperatures (i.e., 25–110 °C) when the CO concentration in the anodic stream is 500 ppm. In other words, in the presence of CO (500 ppm in N$_2$) in the gas phase no vacant Pt sites exist. This justifies, in part, the

Fig. 4. Cyclic voltammograms on Pt composite electrode with N$_2$ in gas phase after exposure to 476 ppm CO in N$_2$ at a flow rate of 0.10 SLM for various exposure times (shown in the legend) and for a clean Pt composite electrode (- - -). The experiments were conducted at 25 °C and 101.325 kPa.
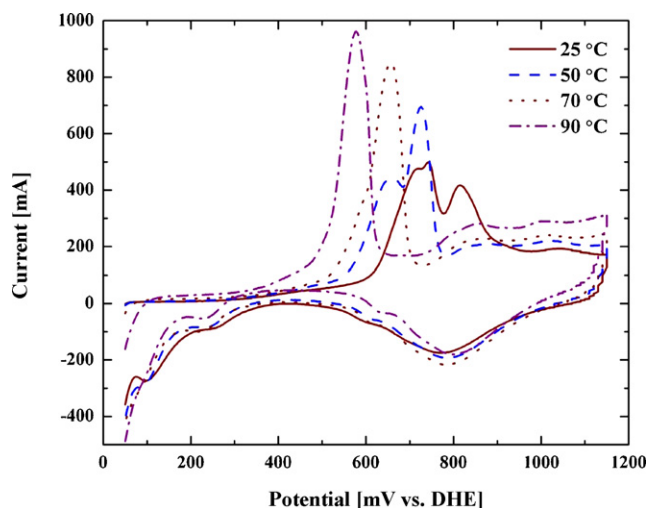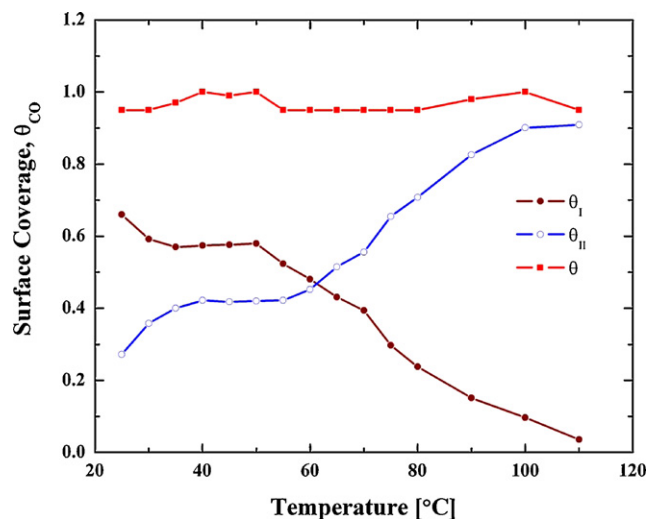

Fig. 6. Experimentally measured surface coverages of CO$_{ad}^I$ (●) and CO$_{ad}^{II}$ (○) as a function of temperature. These data points were obtained by deconvoluting the CVs from the dataset shown in Fig. 5 and using the resulting coulombic charges in Eqs. (2) and (3). The sum of these two coverages (■) was 1 ± 0.05.
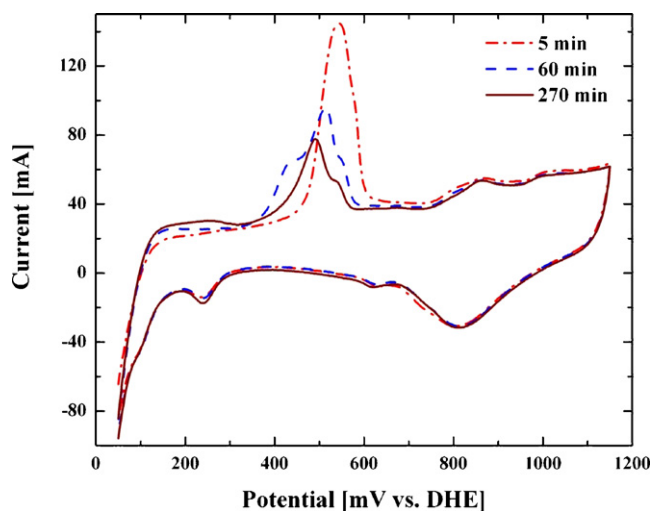
Fig. 7. CVs on a Pt composite electrode under N_2 flow after three sample desorption times. The electrodes were initially exposed to 476 ppm CO in N_2 for 300 s at 95 °C and 101.325 kPa.

Fig. 8. Total surface coverage of CO as a function of desorption time at 95 °C and 101.325 kPa. The data (●) was fit (solid line) to the sum of Eqs. (9) and (10).

applicability of results from well-defined single-crystal studies to our study on Pt nanoparticles (i.e., the assumption of h_I and h_{II} values). An important implication of θ_{CO} being 1 is that the adsorption rate constants cannot be measured using (9) and (10).

Fig. 7 shows CVs on Pt electrode after various desorption times at 95 °C. The peak current and the CO oxidation area decrease with the increase in desorption time confirming considerable desorption of CO molecules in the given period. For example, the peak current decreased from 555 to 447 mA and the peak potential decreased from 542 to 534 mV when the desorption time was increased from 5 to 15 min, respectively. The decrease in peak potential with increasing desorption time can be attributed to the lower surface coverage which enables the formation of oxidative OH species at lower potentials and is consistent with similar observation on single-crystal Pt electrodes by Cuoto et al. [20]. On close inspection, a shoulder growth occurring at potentials lower that the main peak can be seen even for short duration (less than 300 s). Even though there was considerable reduction in the area under the CO peak, there was no corresponding increase in the area under the hydrogen oxidation region suggesting that not much free sites are formed. This could only be explained, if CO_{ad}^{II} were rearranging to CO_{ad}^{I} thereby leading to minimal change in free sites even after considerable decrease in CO area. Therefore, the shoulder occurring at lower potentials was attributed to the increase in the surface coverage of CO_{ad}^{I}.

Fig. 8 shows the overall surface coverage of CO as a function of desorption time at 95 °C. The data points were obtained from the CVs shown in Fig. 7 and the solid line correspond to the least squares fit. The parameter estimation procedure involved solving for the desorption and rearrangement rate constants using Eqs. (9) and (10) together with their initial conditions. The model predictions using the fitted parameters are shown in Fig. 9. The CO_{ad}^{I} (●) and CO_{ad}^{II} (○) surface coverages are indicated as a function of desorption time. The predicted surface coverages for CO_{ad}^{I} and CO_{ad}^{II} compare very well with the individual areas validating the parameter estimation procedure. This also validates the individual surface coverage measurements from the CO peaks observed in the voltammograms and that OH_{ads} formation kinetics did not influence or alter the individual surface coverages. In other words, if OH_{ads} were to influence peak separation (and therefore causing erroneous measurement of individual surface coverages), then desorption and rearrangement parameters estimated using the overall surface coverage data would not have successfully predicted the individual surface coverages. It
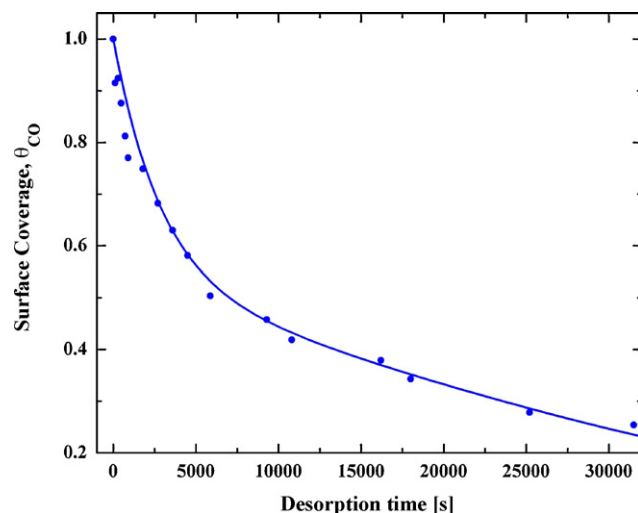
must be noted that the confidence for the rearrangement rate constants was relatively low due to fewer number of data points in the medium range of desorption times.

The parameter estimation routine was repeated for experimental data obtained at temperatures between 50 and 95 °C and the kinetic rate constants were determined. The values and confidence intervals are given in Table 1. Analysis was done in this temperature range because CO desorption was too slow at lower temperatures (i.e., <50 °C). Also, at temperatures higher than 100 °C, deconvoluting the CVs with good confidence tends to be difficult. Fig. 10 shows the Arrhenius plot of the parameters from 50 to 95 °C. The symbols correspond to the different kinetic rate constants as indicated by the legend. The rate constants (symbols) in Fig. 10 was fit to Eq. (11), resulting in

$$k_{-1} = 0.3304 \exp\left(-\frac{24082}{RT}\right), \quad k_{-2} = 0.387 \exp\left(-\frac{27995}{RT}\right),$$

$$k_3 = 8.9484 \exp\left(-\frac{35229}{RT}\right), \quad k_{-3} = 1.8686 \exp\left(-\frac{27550}{RT}\right) \quad (12)$$

The activation energy for desorption of CO_{ad}^{I} and CO_{ad}^{II} were 24.08 and 27.99 kJ/mol, respectively. The activation energy for rear-
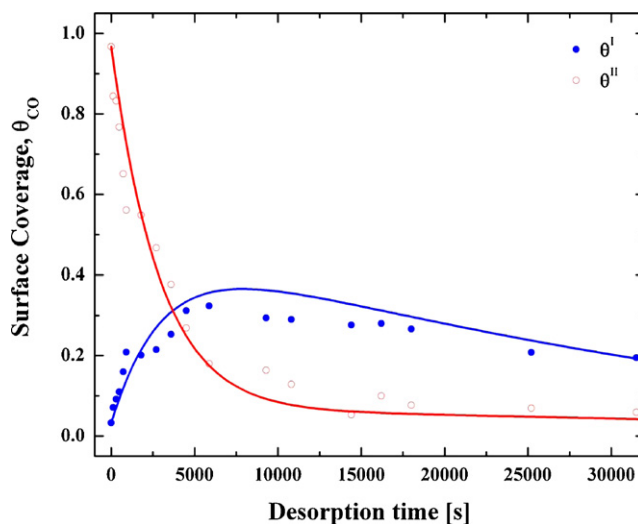

Fig. 9. Surface coverages of CO_{ad}^{I} (●) and CO_{ad}^{II} (○) molecules measured at 95 °C and 101.325 kPa were compared to model predictions.
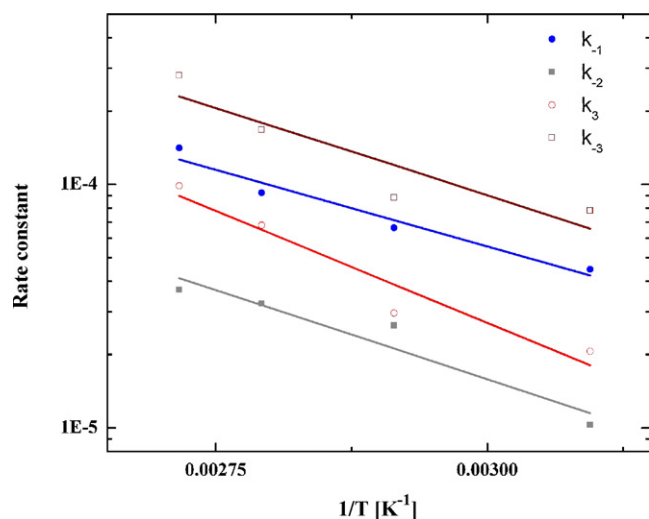
Fig. 10. Arrhenius plots for desorption (k_{-1} and k_{-2}) and rearrangement (k_3 and k_{-3}) rate constants in the temperature range of 50–95 °C. The symbols correspond to the different kinetic constants indicated by the legend. The Arrhenius expressions for each of these rate constants are given in Eq. (12).

rangement from CO_{ad}^{I} to CO_{ad}^{II} was 35.23 kJ/mol and that from CO_{ad}^{II} to CO_{ad}^{I} was 27.55 kJ/mol. The lower activation energy for desorption of CO_{ad}^{I} than CO_{ad}^{II} is consistent with the observation by Markovic et al. [44]. Further, this is also consistent with the spectroscopic data in that CO_{ad}^{I} appears at a lower wave number (indicating weaker adsorption) than CO_{ad}^{II} in the infrared spectrum.

4. Conclusions

A simple procedure to quantify desorption and rearrangement rates of weakly and strongly bound CO molecules (CO_{ad}^{I} and CO_{ad}^{II}) adsorbed at open circuit on a PEM fuel cell electrode was developed. The surface coverage of CO_{ad}^{I} was high at low temperatures and decreased with increasing temperature, while the opposite was true for CO_{ad}^{II}. Desorption and rearrangement rate constants for CO_{ad}^{I} and CO_{ad}^{II} were determined as a function of temperature pertinent to PEM fuel cell operation. Rearrangement from CO_{ad}^{II} to CO_{ad}^{I} was faster than either of the desorption rates over the entire range of temperature studied. The desorption rate of CO_{ad}^{II} was at least an order of magnitude lower than that of CO_{ad}^{I}. The activation energies for desorption of CO_{ad}^{I} and CO_{ad}^{II} were estimated to be 24.08 and 27.99 kJ/mol, respectively. The activation energy for rearrangement from CO_{ad}^{I} to CO_{ad}^{II} was 35.23 kJ/mol and that from CO_{ad}^{II} to CO_{ad}^{I} was 27.55 kJ/mol. Estimation of electro-oxidation rate constants and the application of these constants towards designing an electrochemical CO filter are currently ongoing in our laboratory.

Acknowledgements

Appendix A. Nomenclature

List of symbols

$a, b, \ldots, f$ parameters in the bimodal Gaussian distribution function

CO_{ad}^{I}	CO species contributing to the first anodic peak
CO_{ad}^{II}	CO species contributing to the second anodic peak
E_a	activation energy (J mol^{-1})
h_I	number of Pt sites per CO molecule for CO_{ad}^{I}, 1.34
h_{II}	number of Pt sites per CO molecule for CO_{ad}^{II}, 1.67
I	current (mA)
k_1	adsorption rate constant for CO_{ad}^{I} (cm^3 mol^{-1} s^{-1})
k_{-1}	desorption rate constant for CO_{ad}^{I} (s^{-1})
k_2	adsorption rate constant for CO_{ad}^{II} (cm^3 mol^{-1} s^{-1})
k_{-2}	desorption rate constant for CO_{ad}^{II} (s^{-1})
k_3	forward (from CO_{ad}^{I} to CO_{ad}^{II}) rearrangement rate constant (s^{-1})
k_{-3}	backward (from CO_{ad}^{II} to CO_{ad}^{I}) rearrangement rate constant (s^{-1})
Q_{CO}^{I}	coulombic charge corresponding to the oxidation of CO_{ad}^{I} (C)
Q_{CO}^{II}	coulombic charge corresponding to the oxidation of CO_{ad}^{II} (C)
Q_{CO}	total coulombic charge corresponding to the CO oxidation (C)
Q_H	total coulombic charge corresponding to H$_2$ oxidation (C)
R	universal gas constant (8.314 J mol^{-1} K^{-1})
T	temperature (K)
V	potential (mV vs. DHE)

Greek symbols

θ_{CO}^{I}	surface coverage of CO_{ad}^{I}
θ_{CO}^{II}	surface coverage of CO_{ad}^{II}
θ_v	surface coverage of vacant sites

Superscripts

I	pertaining to weakly bound or peak I
II	pertaining to strongly bound or peak II

Subscripts

ad	adsorbed
CO	carbon monoxide
H	hydrogen
v	vacant sites

References

[1] H.-F. Oetjen, V.M. Schmidt, U. Stimming, F. Trila, J. Electrochem. Soc. 143 (1996) 3838.
[2] Q. Li, R. He, J.-A. Gao, J.O. Jensen, N.J. Bjerrum, J. Electrochem. Soc. 150 (2003) A1599.
[3] G.A. Camara, E.A. Ticianelli, S. Mukerjee, S.J. Lee, J. McBreen, J. Electrochem. Soc. 149 (2002) A748.
[4] A.T. Haug, R.E. White, J.W. Weidner, W. Huang, S. Shi, N. Rana, S. Grunow, T.C. Stoner, A.E. Kaloyeros, J. Electrochem. Soc. 149 (2002) A868.
[5] A.T. Haug, R.E. White, J.W. Weidner, W. Huang, J. Electrochem. Soc. 149 (2002) A862.
[6] C. Korzeniewski, J. Huang, Anal. Chim. Acta 397 (1999) 53.
[7] J. Huang, C. Korzeniewski, J. Electroanal. Chem. 471 (1999) 146.
[8] B. Lakshmanan, W. Huang, J.W. Weidner, Electrochem. Solid State Lett. 5 (2002) A267.
[9] B. Lakshmanan, C. Karuppaiah, U.S. Patent 6,517,963 (2003).
[10] J.-S. McEwen, S.H. Payne, H.J.H.J. Kreuzer, M. Kinne, R. Denecke, H.-P. Steinrück, Surf. Sci. 545 (2003) 47.
[11] H.P. Dhar, L.G. Christner, A.K. Kush, J. Electrochem. Soc. 134 (1987) 3021.
[12] T.E. Springer, T. Rockward, T.A. Zawodzinski, S. Gottesfeld, J. Electrochem. Soc. 148 (2001) A11.
[13] J.J. Baschuk, A.M. Rowe, X. Li, J. Energy Res. Technol., Trans. Am. Soc. Mech. Eng. 125 (2003) 94.
[14] S. Gilman, J. Phys. Chem. 66 (1962) 2657.
[15] S. Gilman, J. Phys. Chem. 67 (1963) 78.
[16] K. Kunimatsu, H. Seki, W.G. Golden, J.G. Gordon II., M.R. Philpott, Langmuir 2 (1986) 464.
[17] J. Sobkowski, A. Czerwinski, J. Phys. Chem. 89 (1985) 365.
[18] B. Beden, C. Lamy, N.R. De Tacconi, A.J. Arvia, Electrochim. Acta 35 (1990) 691.
[19] V.E. Kazarinov, V.N. Andreev, A.V. Shlepakov, Electrochim. Acta 34 (1989) 905.

[20] A. Cuoto, M.C. Perez, A. Rincon, C. Gutierrez, J. Phys. Chem. 100 (1996) 19538.
[21] A. Wieckowski, M. Rubel, C. Gutierrez, J. Electroanal. Chem. 382 (1995) 97.
[22] S.-C. Chang, M.J. Weaver, J. Phys. Chem. 94 (1990) 5095.
[23] S.C. Chang, L.-W.H. Leung, M.J. Weaver, J. Phys. Chem. 93 (1989) 5341.
[24] F. Kitamura, M. Takahashi, M. Ito, Surf. Sci. 223 (1989) 493.
[25] I. Villegas, M.J. Weaver, J. Chem. Phys. 101 (1994) 1648.
[26] D. Kardash, C. Korzeniewski, Langmuir 16 (2000) 8419.
[27] D. Kardash, J. Huang, C. Korzeniewski, Langmuir 16 (2000) 2019.
[28] M. Arenz, K.J.J. Mayrhofer, V. Stamenkovic, B.B. Blizanac, T. Tomoyuki, P.N. Ross, N.M. Markovic, J. Am. Chem. Soc. 127 (2005) 6819.
[29] G.A. Camara, J.F. Gomes, K. Bergamaski, E. Teixeira-Neto, F.C. Nart, J. Electroanal. Chem. 617 (2008) 171.
[30] F. Maillard, E.R. Savinova, U. Stimming, J. Electroanal. Chem. 599 (2007) 221.
[31] O.V. Cherstiouk, P.V. Simonov, V.I. Zaikovskii, E.R. Savinova, J. Electroanal. Chem. 554–555 (2003) 241.
[32] B. Andreaus, F. Maillard, J. Kocylo, E. Savinova, M. Eikerling, J. Phys. Chem. B 110 (2006) 21028.
[33] S. Guerin, B.E. Hayden, C.E. Lee, C. Mormiche, J.R. Owen, A.E. Russell, J. Combust. Chem. 6 (2004) 149.
[34] N.P. Lebedeva, M.T.M. Koper, J.M. Feliu, R.A. van Santen, J. Phys. Chem. B 106 (2002) 12938.
[35] F. Maillard, E.R. Savinova, P.A. Simonov, V.I. Zaikovskii, U. Stimming, J. Phys. Chem. B 108 (2004) 17893.
[36] J. Solla-Gullón, F.J. Vidal-Iglesias, E. Herrero, J.M. Feliu, A. Aldaz, Electrochem. Commun. 8 (2006) 189.
[37] H. Kita, H. Naohara, T. Nakato, S. Taguchi, A. Aramata, J. Electroanal. Chem. 386 (1995) 197.
[38] O.V. Cherstiouk, P.A. Simonov, E.R. Savinova, Electrochim. Acta 48 (2003) 3851.
[39] N.M. Markovic, P.N. Ross, Surf. Sci. Rep. 45 (2002) 117.
[40] K.J.J. Mayrhofer, M. Arenz, B.B. Blizanac, V. Stamenkovic, P.N. Ross, N.M. Markovic, Electrochim. Acta 50 (2005) 5144.
[41] R. Van Hardeveld, F. Hartog, Surf. Sci. 15 (1969) 189.
[42] R. Van Hardeveld, A. Van Montfoort, Surf. Sci. 4 (1966) 396.
[43] K. Kinoshita, J. Electrochem. Soc. 137 (1990) 845.
[44] N.M. Markovic, B.N. Grgur, C.A. Lucas, P.N. Ross, J. Phys. Chem. B 103 (1999) 487.
[45] R. Gómez, J.M. Feliu, A. Aldaz, M.J. Weaver, Surf. Sci. 410 (1998) 48.
[46] N.M. Markovic, V. Radmilovic, P.N. Ross Jr., Physical and electrochemical characterization of bimetallic nanoparticle catalysts, in: A. Wieckowski, E.R. Savinova, C.G. Vayenas (Eds.), Catalysis and Electrocatalysis at Nanoparticle Surfaces, CRC Press, 2003, p. 311.
[47] N.M. Markovic, P.N. Ross Jr., CATTECH 4 (2000) 110.
[48] T.J. Schmidt, P.N. Ross, N.M. Markovic, J. Phys. Chem. B 105 (2001) 12082.
[49] E. Pastor, J.L. Rodriguez, T. Iwasita, Electrochem. Commun. 4 (2002) 959.
[50] T. Patterson, Pre-Print Archive, American Institute of Chemical Engineers, Spring National Meeting, New Orleans, LA, 2002, p. 313.
[51] G.E. Gdowski, R.J. Madix, Surf. Sci. 115 (1982) 524.
[52] M. Heinen, Y.-X. Chen, Z. Jusys, R.J. Behm, Chem. Phys. Chem. 8 (2007) 2484.
[53] J.C. Davies, R.M. Nielsen, L.B. Thomas, I. Chorkendorff, Á. Logadóttir, Z. Lodziana, J.K. Nørskov, W.X. Li, B. Hammer, S.R. Longwitz, J. Schnadt, E.K. Vestergaard, R.T. Vang, F. Besenbacher, Fuel Cells 4 (2004) 309.
[54] A. Constantinides, N. Mostoufi, Numerical Methods for Chemical Engineers with MATLAB Applications, Prentice Hall, Upper Saddle River, NJ, 1999, p. 439.
[55] E. Herrero, J.M. Feliu, Langmuir 16 (2000) 4779.